Chemical Technology and Engineering Applications

https://ctea.cultechpub.com/ctea

Cultech Publishing

Article

Eco-Friendly Synthesis of Ag–Co_3O_4 Nanoparticles for Visible-Light Photocatalysis and DFT-Based Nonlinear Optical Investigation

Muhammad Amir Abbas*, Muhammad Shahid Rasool

Institute of Chemistry, The Islamia University of Bahawalpur, Bahawalpur, Pakistan

*Corresponding author: Muhammad Amir Abbas, muhammadamirabbas@gmail.com

Abstract

Ag–Co_3O_4 nanoparticles were synthesized via an eco-friendly green route using Gum Arabic as a natural biopolymer, serving simultaneously as a reducing and stabilizing agent to enable controlled nanoparticle growth. The as-prepared nanomaterials were investigated for the visible-light-driven photocatalytic degradation of methyl orange (MO). Structural and morphological characterization using X-ray diffraction (XRD) confirmed the formation of a highly crystalline cubic phase with an average crystallite size of approximately 20 nm, which was in good agreement with the nearly uniform particle size observed by scanning electron microscopy (SEM). Ultraviolet-visible diffuse reflectance spectroscopy revealed a reduced optical band gap of 2.09 eV compared to pristine Co_3O_4, indicating enhanced visible-light absorption. Owing to these favorable structural and optical features, the Ag–Co_3O_4 nanoparticles exhibited excellent photocatalytic performance, achieving up to 96% degradation of MO within 3 h under visible-light irradiation at room temperature. To complement the experimental findings, density functional theory (DFT) calculations were carried out at the B3LYP level to examine the electronic structure and nonlinear optical (NLO) properties. The computed frontier molecular orbital (FMO) and charge-transfer characteristics revealed improved electronic delocalization, while significantly enhanced first hyperpolarizability values (β = 11,441.88 and 54,398.78 a.u.) confirmed strong NLO responsiveness. The combined experimental and theoretical results highlight the potential of green-synthesized Ag–Co_3O_4 nanomaterials for advanced photocatalytic and optoelectronic applications.

Keywords

Ag–Co_3O_4 nanoparticles, Green synthesis, Gum Arabic, Photocatalytic degradation, Nonlinear optical, Density functional theory

Article History

Received: 28 December 2025
Revised: 27 January 2026
Accepted: 11 March 2026
Available Online: 23 March 2026

1. Introduction

Nanotechnology has become a revolutionary field because materials at the nanoscale show amazing chemical and physical properties. This is the reason for the enormous research taking place in the synthesis and modification, and application of nanomaterials in various fields, which include catalysis, nanomedicine, pollutant adsorption, and photocatalysis [1-3]. Among many metal oxide nanomaterials, Co_3O_4 has been given significant attention because it is inexpensive, naturally abundant, chemically stable, and possesses multifunctional properties [4]. Co_3O_4 is a p-type semiconductor with a cubic spinel structure; Co^{2+} ions are found at tetrahedral sites, while Co^{3+} ions are at octahedral sites. Such an arrangement of atoms provides good electronic properties to this compound, which possesses an optical bandgap of about 3.95-2.13 eV [5-8].

Due to its unique structural and electronic features, Co_3O_4 has been widely explored in organic synthesis, supercapacitors, water-splitting reactions, and photocatalytic degradation of organic pollutants [9-13]. However, pristine Co_3O_4 is severely plagued by quick charge carrier recombination and limited visible-light absorption, thereby seriously jeopardizing its photocatalytic efficiency. To overcome these drawbacks, noble metal incorporation, particularly silver (Ag), has been demonstrated as an effective strategy to enhance charge separation, improve light harvesting, and promote interfacial electron transfer, thereby significantly improving photocatalytic performance.

Co_3O_4 nanoparticles are normally fabricated via hydrothermal, sol-gel, sonochemical, and co-precipitation methods. In most cases, these methods have major drawbacks, such as excessive energy consumption, toxic chemicals, and hazardous conditions [14-17]. Alternatively, the green synthesis methods include plant extracts, biopolymers, and microorganisms, and their interest has significantly increased, due to their compatibility with the environment, low cost, simplicity, and reduced production of hazardous waste [18-22]. Among different biopolymers, one should consider Gum Arabic (Acacia gum) due to its rich polysaccharide content and abundance of functional groups, which enable it to act simultaneously as reducing, stabilizing, and templating agent in one step for nanoparticles.

The huge amount of synthetic dyes polluting the water bodies has enhanced the environmental significance of this work. Methyl orange (MO) is one such popular azo dye, which is toxic, chemically stable, and resistant to biodegradation, hence posing serious threats to aquatic ecosystems and human health [23-25]. Photocatalytic degradation has emerged as one of the efficient and sustainable approaches out of the available techniques for dye removal, which include adsorption, electrochemical treatment, and biodegradation due to its low energy requirements, high efficiency, and little secondary pollution [26-35]. Within this context, the current study discusses the green synthesis of Ag–Co_3O_4 nanoparticles by using Gum Arabic as a biopolymer. This is followed by extensive structural, morphological, and optical characterizations. The photocatalytic efficiencies of the synthesized nanomaterials are systematically assessed toward the degradation of MO under visible-light irradiation. Also, electronic structure and nonlinear optical (NLO) properties of the Ag–Co_3O_4 are investigated by means of density functional theory (DFT) calculations. Integration of experimental photocatalytic performance with theoretical considerations thus provides valuable insight into charge-transfer behavior, modulation of bandgap, and optoelectronic potential. Such a combined experimental-computational approach establishes the Ag–Co_3O_4 nanomaterials with multifunctional usability in environmental remediation and advanced optoelectronic devices.

2. Experimental Section

2.1 Materials

Gum Arabic (Acacia gum) was obtained from a certified bio-shop. Silver nitrate and Cobalt nitrate hexahydrate ($Co(NO_3)_2{\cdot}6H_2O$) was procured from Merck and used as such without further purification. MO dye served as a model pollutant for photocatalytic studies. All aqueous solutions were prepared using double-distilled water [36].

2.2 Green Synthesis of Co_3O_4 Nanoparticles

One gram of $AgNO_3$ and Co $(NO_3)_2{\cdot}6H_2O$ was added to the biopolymer solution under continuous stirring after preparation of the Gum Arabic solution according to the reported method [36]. After that, the reaction mixture was kept at 70 °C for 10 h until it became dry gel. The dried precursor calcined at 500 °C for 4 h yielded crystalline Ag–Co_3O_4 nanoparticles.

2.3 Photocatalytic Degradation Experiments

The photocatalytic activity was tested for MO degradation under visible light irradiation using a batch photo-reactor fitted with a fluorescent lamp. It explores the effect of three variables: initial dye concentration (5-15 mg/L), catalyst dosage (0.02-0.04 g), and time of irradiation. Then, the centrifuged solution was analyzed for its absorbance at λmax = 457 nm on a UV-Vis spectrophotometer.

2.4 Computational Methodology

All advanced computer simulations have been performed using DFT calculations, such as geometry optimization,

frontier molecular orbital (FMO) analysis, computation of global quantum chemical descriptors, molecular electrostatic potential (MESP)mapping, as well as calculations for first hyperpolarizabilities. These diverse theoretical calculations together elucidate tremendous charge transfer properties as well as elevated electronic polarization capabilities of the Ag–Co_3O_4 system, which are largely acknowledged as significant markers of NLO properties. Significantly, these DFT calculations together elucidate mechanistic properties to interpret the experimental photocatalytic properties, as well as confirm multifunctional capabilities of Ag–Co_3O_4 nanoparticles beyond pollutant cleanup.

3. Results and Discussion

3.1 Fourier Transform Infrared (FTIR) Analysis

Figure 1 shows the FTIR spectra of Ag–Co_3O_4 in the range of 4000-450 cm^{-1}. The broad absorption peak in the interval 3453-3369 cm^{-1} is associated with O–H stretching frequencies due to adsorbed hydroxyl groups and physically adsorbed water molecules on the metal oxide phase. The weaker peak observed in the vicinity of 2120 cm^{-1} may be related to overtone or combination bands. The peak at 1708 cm^{-1} is associated with H–O–H bending modes of molecular water or adsorbed carbonyl functionalities on the surfaces. The peaks at 1632 cm^{-1} and 1607 cm^{-1} are attributed to bending vibrations of the hydroxyl groups on the surface. These are signs of chemisorbed –OH groups acting as active sites. The peaks recorded at 1498 cm^{-1} and 1442 cm^{-1} could be attributed to the carbonate ion (CO_3^{2-}) formed as a result of the adsorption of atmospheric CO_2. In the fingerprint area, the major bands assigned between 1364 and 1121 cm^{-1} are due to C–O bonds and Co–O–H vibrations, representative of surface hydroxylation and lattice effects. Bands in the area 1049-825 cm^{-1} can be assigned to metal-oxygen stretching vibrations, validating the formation of cobalt-oxygen networks. Significantly, major bands corresponding to 608, 543, and 502 cm^{-1} can be assigned to metal-oxygen vibrations, specifically witnessing Co–O vibrations, definitely establishing the presence of Ag–Co_3O_4 in the crystal phase. As a whole, the FTIR analysis verifies the successful preparation of the cobalt oxide with hydroxyl and carbonate groups, which, in turn, is helpful for improving adsorption capacity and catalytic activities [37].

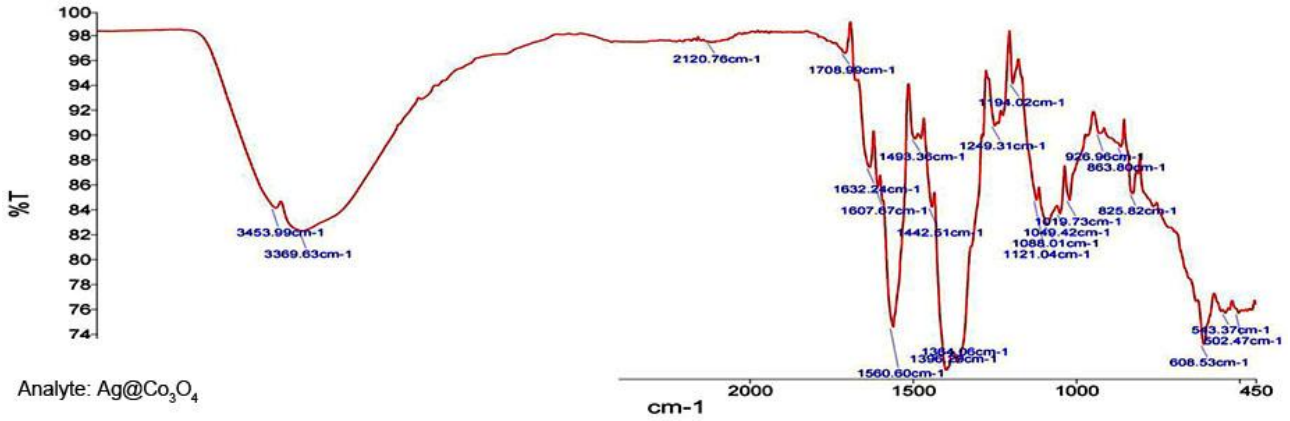

Figure 1. FTIR spectrum of green-synthesized Ag–Co_3O_4 nanomaterials. The spectrum shows characteristic metal-oxygen (Ag–O and Co–O) vibrations and surface functional groups responsible for nanoparticle stabilization.

3.2 X-Ray Diffraction (XRD) Analysis

XRD analysis was conducted to investigate the crystal structure and phase purity of the prepared Ag–Co_3O_4 nanoparticles. The diffractogram showed in Figure 2 well-defined characteristic peaks corresponding to the cubic spinel structure of Ag–Co_3O_4, which agreed well with standard Joint Committee on Powder Diffraction Standards (JCPDS) data and confirmed successful formation of the crystalline phase. No additional peaks from impurities were observed, indicating high phase purity for the synthesized material. Estimated average crystallite size according to the Scherrer equation was found to be around 20 nm. This is strictly a size that represents the coherent diffracting domain and not the physical particle size, which should be clearly differentiated in any microscopic observation. The difference in crystallite size as calculated by XRD and the particle size estimated by SEM may be due to the agglomeration of particles and also to the polycrystalline nature of the nanoparticles where each particle is made up of many crystallites fused together [38,39].

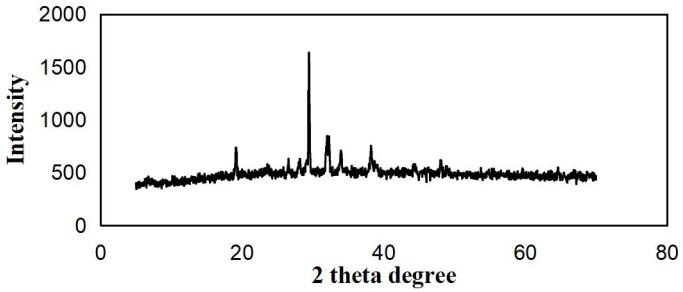

Figure 2. XRD pattern of Ag–Co_3O_4 nanomaterials. The pattern shows a cubic crystal structure and high crystalline; the average crystallite size (~20 nm) was estimated using the Scherrer equation.

3.3 UV-Visible Diffuse Reflectance Spectroscopy (UV-Vis DRS)

The optical properties of Ag–Co_3O_4 nanoparticles were studied by using UV-Vis DRS. The obtained absorption spectrum showed strong and extended absorption in the visible region, and the calculated optical bandgap was 2.09 eV. This reduced bandgap compared to pristine Co_3O_4 could be due to the incorporation of Ag, which promotes improved charge transfer and introduces localized electronic states within the host band structure. In this regard, Figure 3 indicate the narrowing bandgap can enhance visible-light harvesting capability, which is an important factor for efficient photocatalytic process applications. Therefore, it is clear that the extent of the absorption in the visible-light region strongly supports the suitability of Ag–Co_3O_4 nanoparticles in photoinduced processes under solar irradiation [40].

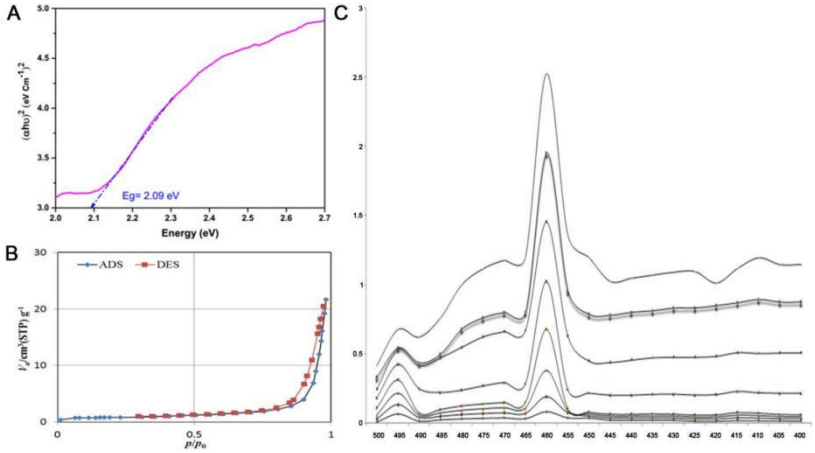

Figure 3. Optical and physicochemical characterization of Ag–Co_3O_4 nanomaterials. (A) Tauc plot obtained from UV–Vis diffuse reflectance data, indicating an optical band gap of approximately 2.09 eV, which suggests improved absorption in the visible-light region. (B) Nitrogen adsorption–desorption (ADS/DES) isotherm demonstrating the porous nature and surface properties of the prepared nanomaterial. (C) Raman spectra displaying the characteristic vibrational bands of Co_3O_4, confirming the crystalline structure and the successful integration of Ag within the material framework.

3.4 Scanning Electron Microscopy (SEM) and Energy Dispersive X-ray Spectroscopy (EDX) Analysis

SEM analysis indicates in Figure 4, the major morphology of the Ag–Co_3O_4 nanoparticles is octahedral, with an average particle size of around 20 nm. However, agglomeration to some extent was observed in line with the high surface energy and magnetic interactions between nanoscale particles. Elemental mapping further confirmed the homogenous distribution of the elements, namely cobalt and oxygen, which also justifies the composition purity of the prepared cobalt oxide frame and confirms the successful incorporation of Ag without altering the main crystal structure.

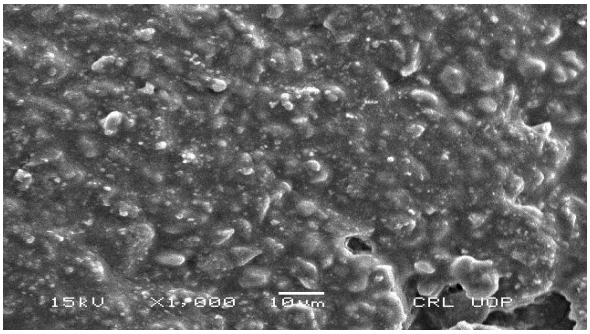

Figure 4. SEM micrograph of Ag–Co_3O_4 nanomaterials. The image reveals nearly spherical morphology with slight agglomeration and an average particle size in the nanometer range.

3.5 Investigation of Kinetics

The heterogeneous catalyzed reactions are highlycomplex in nature. The cause for this complexity is the simultaneous adsorption of reactant molecules and the desorption of product molecules. The rate expression for the complex reaction could be simplified on the basis of certain assumptions, which are Quasi-equilibrium, and Hypothesis, also referred to as Quasi-Steady-State Hypothesis. The rate expression for MO degradation was designated by utilizing the Power rate law as shown in equation (1).

$$\text{Rate}=k\,[MO]^{a}[O_2]^{b} \quad \ldots..(1)$$

Partial pressure of oxygen equation (1) kept constant then following equation obtained equation (2):

$$\text{Rate} = k\,[MO]^{a} \quad \ldots..(2)$$

Where

k = the rate constant.

a = Order of reaction of rhodamine B.

b = Order with respect to oxygen.

Assuming pseudo-first-order kinetics, the rate law can be expressed as equation (3):

$$-\frac{d[MO]}{dt}=k[MO] \quad \ldots..(3)$$

Rearranging equation (3) gives equation (4):

$$-\frac{d[MO]}{[MO]}=kdt \quad \ldots..(4)$$

Integrating equation (4) from initial concentration $[MO]_o$ at t = 0 to $[MO]_t$ at time t yields equation (5):

$$\int_o^t \frac{d[MO]}{[MO]}=k\int_o^t dt \quad \ldots..(5)$$

Performing the integration results in equation (6):

$$ln\frac{[MO]_o}{[MO]_t}=kt \quad \ldots..(6)$$

Here

$[MO]_o$= The MO with initial concentration.

$[MO]_t$= The MO with concentration at time t.

The plot of equation 6 based on experimental data at varying temperatures is shown in Figure 5. From the kinetics study, straight lines represent pseudo first order reaction. The slope of straight lines provides the value of rate constants and from the slope of straight lines in Figure 7, values of rate constants are presented in Table 1.

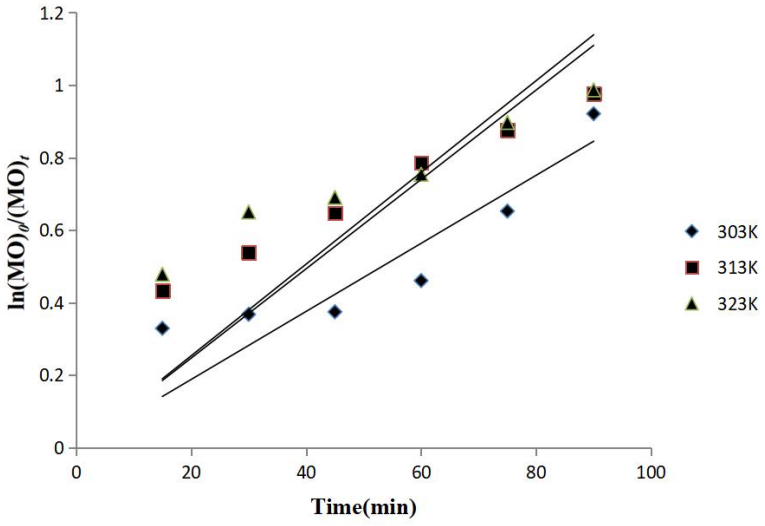

Figure 5. Pseudo-first-order kinetic plots for the photocatalytic degradation of methylene orange (MO) over Ag–Co_3O_4/MOF at different temperatures (303 K, 313 K, and 323 K). The linear relationship between $\ln(MO_0/MO_t)$ and reaction time indicates that the degradation process follows pseudo-first-order kinetics. The increase in slope with rising temperature suggests enhanced reaction rates and improved catalytic activity at higher temperatures.

Table 1. Rate constant determined by application of Eq 6 to Ag–Co_3O_4 catalyzed degradation of MO at various temperatures.

Temperature (K)	Rate Constant(min^{-1})
303	0.009
313	0.012
323	0.019

Similarly, equation 6 was applied to Ag–Co_3O_4 catalyzed degradation of MO with different initial concentrations 100, 200 and 300ppm. The application of equation 6 to experimental data is given in Figure 6. The straight lines indicate the applicability of equation to data. The rate constant with different concentrations of MO dye determined from the slopes of a straight line are given in Table 2.

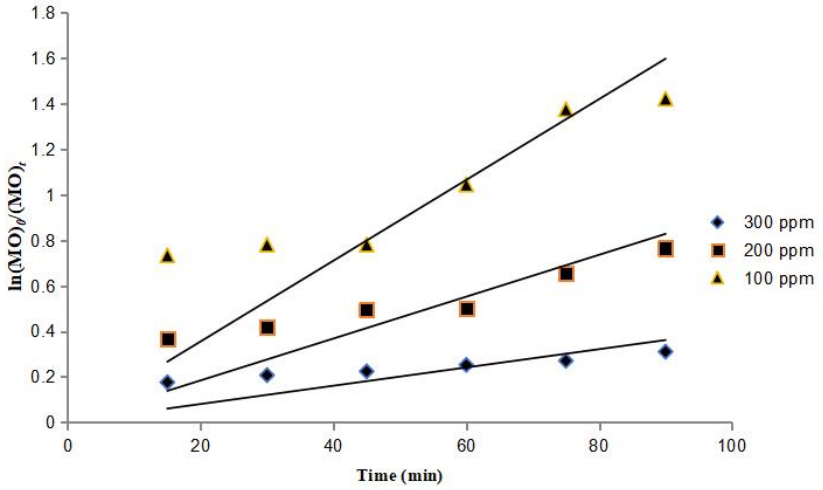

Figure 6. Application of Eq 6 to Ag–Co_3O_4catalyzed degradation of MO at various concentrations.

Table 2. Rate constant confirmed by application of Eq 6 to Ag–Co_3O_4 catalyzed MO degradation at various concentrations.

Concentration in (ppm)	Rate Constant(min^{-1})
100	0.004
200	0.009
300	0.017

3.6 Energy of Activation

It is well established that the rate of reaction increases to an appreciable extent with a rise in temperature. Experimentally, it has been found that for a 10℃ rise in temperature, the velocity of reaction is doubled or trebled. Arrhenius equation (7) explains the effect of temperature on the rate of reaction. The rate constant "k" changes by changing the temperature. According to Arrhenius.

$$k = A\ e^{-Ea/RT} \quad \ldots\ldots(7)$$

So 'k' is exponentially related to energy of activation Ea and temperature, T and R is general gas constant, and e is the base of logarithm. The equation shows that the rate of reaction increased by increasing temperature and the reaction of high activation energy has low 'k' values. The factor 'A' is called Arrhenius constant and it depends upon the collision frequency of reacting substances. The Arrhenius plot is shown in Figure 7. From the slop of Arrhenius graph energy of activation was calculated and was found 30.31 $kJmol^{-1}$.

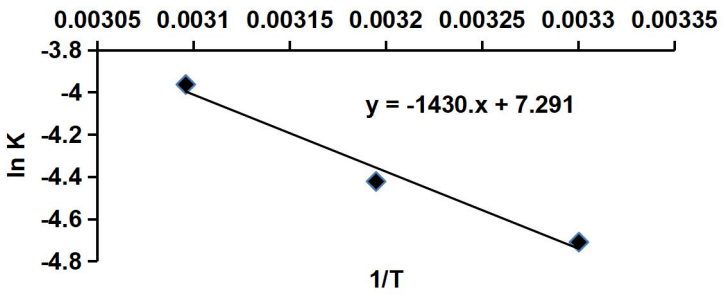

Figure 7. Arrhenius plot for Ag–Co_3O_4 catalyzed photo degradation of MO.

3.7 Mechanism of Reaction

When radiation falls on the catalyst, the electron will absorb radiation and get excited with the formation of a positive hole (e–/h+). This mechanism is called photo catalytic degradation mechanism. Oxygen adsorbed on the surface of the catalyst and takes up electron, it is converted into superoxide anion (O_2^-). This superoxide anion reacts with water molecule and is converted into OH radicals. It was observed that positive hole produced in valence band of catalyst and OH radical produces by reacting with water. These active radicals have much more significance to mineralization the pollutants. When 'Ag' doped on Co_3O_4 the photo catalytic activity of Co_3O_4 enhances. Ag nano particle doped on Co_3O_4 act as trapper for photo excited electrons. The well-known Schottky effect explain electron-positive hole pair avoids from the re-union.

$Ag–Co_3O_4 + hv\ (visible\ light) \rightarrow e^-_{CB} + h^+_{VB}$ *(Photo excitation under visible light)*

$e^-_{CB}(Co_3O_4) \rightarrow e^-(Ag)$ *(Electron transfer to Ag (charge separation))*

$e^- + O_2 \rightarrow \cdot O_2^-$ *(Formation of superoxide radicals)*

$h^+ + H_2O \rightarrow \cdot OH + h^+$ *(Formation of hydroxyl radicals)*

$\cdot O_2^- / \cdot OH + dye\ (MO) \rightarrow oxidative\ products\ (intermediates) \rightarrow CO_2 + H_2O + (inorganic\ ions)$

$MO\ (dye) \rightarrow H_2O + CO_2 + NH_4^+ + NO_3^- + SO_4^{2-}$ *(Final mineralization products)*

3.8 Photocatalytic Degradation of MO

Photocatalytic tests showed the decolorization efficiency of 14% (photolysis), 43% (adsorption), and 96% (photocatalysis), proving the prevailing importance of the photocatalytic oxidation mechanism. An increase in the amount of the catalyst led to an improvement in the efficiency of decolorization, although an increase in the dye concentrations decreased decolorization. Complete decolorization (96%) was accomplished within a short duration of 3 h. The structural and optical properties of the Ag–Co_3O_4 nanoparticles can thus be directly related to their enhanced photocatalytic performance. Specifically, the crystallinity of the material contributes to good charge transport, while its narrowing bandgap and expanded visible-light absorption allow for the increased generation of electron-hole pairs under visible light irradiation. Moreover, Ag impurities provide electron sinks for charge carriers, hindering the recombination of these charge carriers and further increasing photocatalytic efficiency. In conclusion, these synergistic effects explain the excellent photocatalytic degradation performance obtained experimentally and lighten the role of structural engineering in optimizing photocatalytic activity.

4. Computational Advances for NLO Processes

The complementary DFT analysis performed with FMO, NBO, and hyperpolarizability calculations showed high charge transfer and increased electronic polarization. Such properties are a clear intimation of high NLO response, warranting the experimental observation and furthering the application capacity of Ag–Co_3O_4 nanoparticles from contaminant remediation.

4.1 DFT Geometry Optimization: Bond Length and Bond Angle Analysis

DFT geometry optimization was carried out to interpret structural variation occurring in pristine MO as well as in the Ag–Co_3O_4@MO composite. Optimized values of bond lengths, as well as bond angles, help in understanding direct electronic redistribution, metal-oxide coupling, as well as intermolecular interaction.

4.1.1 MO

In the isolated MO structures, the optimized geometry retains the conjugated aromatic system as predicted. The C–C bond lengths in the aromatic rings measure 1.38 to 1.42 Å, as expected for a π-bonded system with delocalized electrons. The C–N and N–N bonds, such as C–N bonds = 1.37 to 1.48 Å, N–N bonds = 1.30 Å, show partial double bond character as a result of resonance between the azo and ammonia functional groups. S-O bond distances (roughly 1.64-1.59 Å) and the S–Na bond (about 2.75 Å) reflect the ionic character of the sulfonate moiety, whereas O–S–O bond angles (roughly 52-53°) and C–S–O bond angles (approximately 125-128°) do not represent tetrahedral geometry due to the asymmetry in the negative charge distribution and sodium coordination. The bond angles around sp^2 carbons are found to be close to the ideal value of 120°, thus retaining planarity and conjugation in the molecule.

4.1.2 Ag–Co_3O_4@MO Composite

Interaction with Ag–Co_3O_4 causes discernible geometric distortions for MO. Some C–C and C–N bonds are revealed to slightly extend (C–C ≈ 1.39-1.42 Å; C–N ≈ 1.39-1.45 Å), reflecting the allocation of electron density in the charge transfer process between the MO molecules and the metal oxide surface. The S–O and S–C bonds extending up to ≈ 1.68 Å for S–O and ≈ 1.85 Å for S–C also reflect high coordination between the sulfonate group and metal ions, thereby reducing the initial covalent bonds. New metal-oxygen and metal-chloride bonds are definitely formed, for example,

Co–O (1.56-1.60 Å) and Ag–Co (2.50 Å), which rule out physisorption. These bonds also impose geometrical restrictions, which lead to the consequent distortion of the surrounding bond angles. For example, angles like O–Co–O (142°) and Co–O–Ag (87°) differ from the ideal angles of an octahedral and tetrahedral geometry, respectively.

The measured variations in bond length and bond angles from those in pristine MO and in the Ag–Co_3O_4@MO composite, as listed in Table S_1, are mainly attributed to the evident electronic and geometric coupling effects at the organic-inorganic interface. Upon adsorption, there is considerable charge transfer from the electron-donating functional groups in the MO molecule to the Ag–Co_3O_4 surface, causing a reduction in bond order for donor bonds and resulting in marked bond lengthening. Concurrently, binding of the MO molecule through sulfonate and azo groups also triggers geometricrestrictions that cause reorientation of these functional groups, thereby causing bond angles to deviate from their expected sp^2 or tetrahedral structures. In addition, steric repulsion and electrostatic interactions between the dye molecule and the metal oxide surface also contribute to further geometric distortions. Roles of hybridization changes in the vicinity of coordination sites also contribute significantly to bond angle variations. In effect, such geometric variations provide affine evidence for the existence of substantial electronic coupling effects in the interaction of the Ag–Co_3O_4 surface and the MO molecule, thereby favoring high degrees of charge delocalization and coupling. Geometric effects that favor efficient charge separations and also highly enhance nonlinear polarization effects are highly desirable in the context of both photocatalytic activity and NLO properties.

4.2 FMOAnalysis and Global Quantum Reactivity Descriptors

The FMO analysis of Figure 8 and Table S_2 gives fundamental insights on the electronic reactivity and charge-transfer behavior of MO and Ag–Co_3O_4@MO hybrid system. In the isolated MO molecule, the energies of HOMO and LUMO have been calculated as -5.24 and -2.02 eV, respectively, with an energy gap ($\Delta E_{(gap)}$) of 3.22 eV. Both the frontier orbitals were stabilized upon interaction with Ag–Co_3O_4, shifting the HOMO to -5.80 eV and LUMO to -2.69 eV, associated with a concomitant decrease in energy gap to 3.11 eV. This reduction in HOMO-LUMO gap points toward improved electronic delocalization and facile intramolecular/interfacial charge transfer within Ag–Co_3O_4@MO system, which itself is one of the prime requirements for enhanced photocatalytic and NLO.

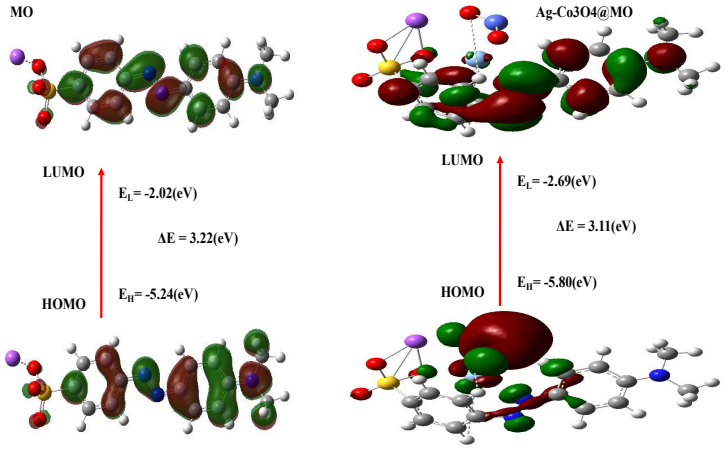

Figure 8. DFT-derived FMO energies of MO and Ag–Co_3O_4@MO.

This trend of behavior can also be clearly observed in the global reactivity descriptors. Entering the composite system, the ionization potential has been found to rise from 5.24 eV for MO to 5.80 eV for the Ag–Co_3O_4@MO composite. This clearly indicates an increase in its resistance to electron loss. But at the same time, its electron affinity (EA), which was 2.02 eV for MO, increases to 2.69 eV for the composite. This clearly indicates an increase in the electron acceptance ability of the composite material. Its electronegativity (χ) value has been observed to increase in magnitude for the composite material. The η values slightly decline from 1.61 eV in MO to 1.56 eV in Ag–Co_3O_4@MO, while the S values increase. The negative trends in the above two parameters clearly denote the electronically softer nature of the hybrid material. Most prominently, the electrophilicity index values increase considerably from 4.09 eV in MO to 5.78 eV in Ag–Co_3O_4@MO. This clearly indicates the enhanced electron-accepting capacity of the Ag–Co_3O_4@MO nanocomposite duo to greater polarization capability. The primary reason behind this increase in η values is the high NLO efficiency.

4.3 MESP Analysis

The MESP study in figure 9 provides additional insights into the charge distribution on the molecular surface, supplementing the FMO study. The MESP study suggests for MO molecules, where the negative potential regions are mainly localized around the sulfonate oxygen and azo nitrogen atoms, while positive regions are distributed over the aromatic hydrogen atoms. The effect in the Ag–Co_3O_4@MO system indicates large intensified regions around the sulfonate oxygen and azo nitrogen atoms, signifying large charge transfer from the MO molecules to Ag–Co_3O_4. The study suggests for Ag–Co_3O_4@MO, where the reduced energy gap, lower hardness, higher softness, and large

electrophilicity index unambiguously show the hybrid system to be more chemically reactive, more polarizable, and electronically more preferable for the applications involving charge-transfer mechanism compared to the individual MO molecules.

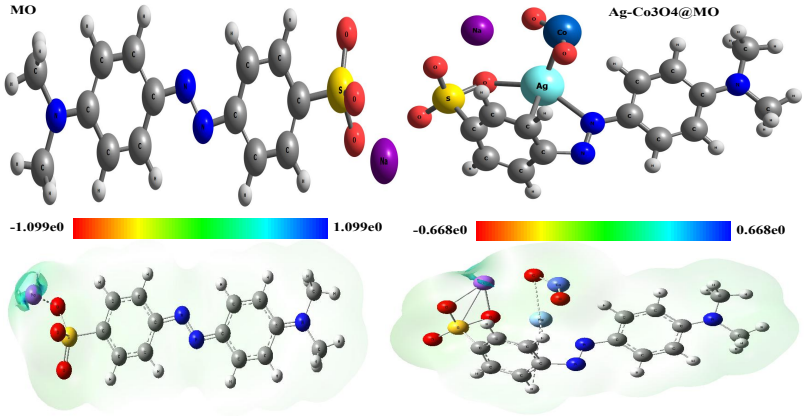

Figure 9. DFT-derived optimized geometries and MESP of MO and Ag–Co_3O_4@MO.

4.4 NLO Behavior and Effect of Ag–Co_3O_4 Coupling

The DFT calculations also confirm that there is an observable increase in the NLO properties of MO upon its interaction with Ag–Co_3O_4. There is an appreciable rise in the dipole moment from 8.08 Debye in free MO to 11.78 Debye in Ag–Co_3O_4@MO, thereby manifesting higher charge asymmetry/polarization caused by metal-oxide interactions. A simultaneous rise in the average polarizability (α) also indicates increased deformability of the electronic cloud with regard to the extended charge delocalization at the organic-inorganic interface. In particular, the value of the first hyperpolarizability β, which is a prominent marker for second-order NLO properties, is increased by a factor of approximately 4.8 after Ag–Co_3O_4 incorporation. The reason for this considerable enhancement is mainly due to efficient intra- and intermolecular charge-transfer transitions from MO to Ag–Co_3O_4 clusters, decreased stiffness in the electronic structure, and increased donor-acceptor interactions. In general, the great improvement in μ, α, and particularly β values significantly verifies the fact that Ag–Co_3O_4 functionalization enhances the MO material into an improved NLO-sensitive medium, thus verifying the application potential of MO in optoelectronic devices, frequency doubling materials, and photonic modulation technologies.

5. Conclusion

In this study, Ag–doped Co_3O_4 nanoparticles were synthesized through an environmentally benign and cost-effective green route using Gum Arabic as a renewable biopolymer that simultaneously functions as a reducing and stabilizing agent. Structural and morphological investigations confirmed the formation of highly crystalline cubic spinel Ag–Co_3O_4 nanoparticles with uniform dispersion, features that are favorable for photocatalytic applications. Optical characterization revealed a reduced optical band gap of 2.09 eV compared to pristine Co_3O_4, leading to improved visible-light absorption and enhanced photocatalytic performance. Under visible-light irradiation at room temperature, the Ag–Co_3O_4 system achieved up to 96% degradation of MO, demonstrating its effectiveness for aqueous pollutant removal under mild operating conditions. Complementary DFT calculations were employed to provide molecular-level insight into the electronic and NLO behavior of the system. Importantly, the DFT-derived HOMO-LUMO energy gap, which reflects electronic reactivity and charge-transfer propensity at the molecular scale, was analyzed independently from the experimentally determined optical band gap. FMO analysis and global quantum descriptors indicated enhanced electronic softness, electrophilicity, and polarization upon interaction with the dye molecule. Furthermore, a pronounced increase in dipole moment, mean polarizability, and first hyperpolarizability highlighted the strong NLO response of the Ag–Co_3O_4 system. Overall, the revised findings demonstrate that green-synthesized Ag–Co_3O_4 nanoparticles represent a multifunctional material platform that combines efficient visible-light photocatalytic activity with favorable electronic and NLO properties. The integrated experimental–computational approach adopted in this work provides a robust framework for the rational design of sustainable nanomaterials for environmental remediation and advanced optoelectronic applications.

Author Contributions

M.A.A wrote the main manuscript Draft, writing, studied Data validation and Editing, Reviewing. All authors reviewed the manuscript outline.

Conflict of Interest

The authors declare that they have no competing interests.

Generative AI Statement

The authors declare that no Gen AI was used in the creation of this manuscript.

References

[1] Dijoo ZK, Khurshid R. Environmental degradation as a multifaceted consequence of human development. Environmental Biotechnology. Palm Bay: Apple Academic Press, 2022, 39-56.

[2] Saxena V. Water quality, air pollution, and climate change: Investigating the environmental impacts of industrialization and urbanization. Water, Air, & Soil Pollution, 2025, 236(2), 73. DOI: 10.1007/s11270-024-07702-4

[3] Ganivet E. Growth in human population and consumption both need to be addressed to reach an ecologically sustainable future. Environment, Development and Sustainability, 2020, 22(6), 4979-4998. DOI: 10.1007/s10668-019-00446-w

[4] Akhtar MS, Ali S, Zaman W. Innovative adsorbents for pollutant removal: Exploring the latest research and applications. Molecules, 2024, 29(18), 4317. DOI: 10.3390/molecules29184317

[5] Rath P, Jindal M, Jindal T. A review on economically-feasible and environmental-friendly technologies promising a sustainable environment. Cleaner Engineering and Technology, 2021, 5, 100318. DOI: 10.1016/j.clet.2021.100318

[6] Haq I, Kalamdhad AS. Advanced and ecofriendly technologies for the treatment of industrial wastewater to constrain environmental pollution. Innovations in Environmental Biotechnology. Singapore: Springer Nature Singapore, 2022, 561-573. DOI: 10.1007/978-981-16-4445-0_22

[7] Bharagava RN. Emerging eco-friendly green technologies for wastewater treatment. Berlin, Heidelberg: Springer, 2020.

[8] Singh V, Ahmed G, Vedika S, Kumar P, Chaturvedi SK, Rai SN, et al. Toxic heavy metal ions contamination in water and their sustainable reduction by eco-friendly methods: Isotherms, thermodynamics and kinetics study. Scientific Reports, 2024, 14(1), 7595. DOI: 10.1038/s41598-024-58061-3

[9] Shamshad J, Rehman RU. Innovative approaches to sustainable wastewater treatment: A comprehensive exploration of conventional and emerging technologies. Environmental Science: Advances, 2025, 4(2), 189-222. DOI: 10.1039/D4VA00136B

[10] Zahan MS, Munshi MR, Rana MZ, Al Masud M. Theoretical insights on geometrical, mechanical, electronic, thermodynamic and photocatalytic characteristics of $RaTiO_3$ compound: A DFT investigation. Computational Condensed Matter, 2023, 36, e00832. DOI: 10.1016/j.cocom.2023.e00832

[11] Manikandan I, Perumal MV, Jayamoorthy K. Synthesis, characterization, physico-chemical and DFT studies of potential organic NLO materials: Experimental and theoretical combined study. Silicon, 2019, 11(1), 425-435. DOI: 10.1007/s12633-018-9837-9

[12] Ahmed TY, Aziz SB, Dannoun EMA. New photocatalytic materials based on alumina with reduced band gap: A DFT approach to study the band structure and optical properties. Heliyon, 2024, 10(5), e27029. DOI: 10.1016/j.heliyon.2024.e27029

[13] Ullah HMN, Rizwan M, Zahid U, Imran A, Cao C. A comprehensive DFT study of physical and photocatalytic properties of Sr1-xCdxTiO_3. Materials Today Communications, 2022, 33, 104495. DOI: 10.1016/j.mtcomm.2022.104495

[14] Hassan AU, Sumrra SH, Zubair M, Mustafa G, Noreen S, Imran M. Correlating the charge density and structural fabrication of new organic dyes to create visible light harvesting materials with tunable NLO refining: Insights from DFT. Chemical Papers, 2023, 77(10), 6183-6202. DOI: 10.1007/s11696-023-02931-z

[15] Khan W, Tariq A, Minar J, Durrani S, Raziq A, Azam S, et al. Band structure engineering, optical, transport, and photocatalytic properties of pristine and doped $Nb_3O_7(OH)$: A systematic DFT study. RSC Advances, 2025, 15(4), 2452-2460. DOI: 10.1039/D4RA08019J

[16] Latif A, Latif A, Mohsin M, Bhatti IA. Density functional theory for nanomaterials: Structural and spectroscopic applications-a review. Journal of Molecular Modeling, 2025, 31(8), 211. DOI: 10.1007/s00894-025-06431-7

[17] Lalithambika KC, Shanmugapriya K, Sriram S. Photocatalytic activity of MoS_2 nanoparticles: An experimental and DFT analysis. Applied Physics A, 2019, 125(12), 817. DOI:B10.1007/s00339-019-3120-9

[18] Zhao Y, Zhang S, Shi R, Waterhouse GI, Tang J, Zhang T. Two-dimensional photocatalyst design: A critical review of recent experimental and computational advances. Materials Today, 2020, 34, 78-91. DOI: 10.1016/j.mattod.2019.10.022

[19] Hamad H, Elsenety MM, Sadik W, El-Demerdash AG, Nashed A, Mostafa A, et al. The superior photocatalytic performance and DFT insights of S-scheme CuO@ TiO_2 heterojunction composites for simultaneous degradation of organics. Scientific Reports, 2022, 12(1), 2217. DOI: 10.1038/s41598-022-05981-7

[20] Abbas MA, Mahar J, Hameed N, Rasool MS. DFT-guided design of a low-band-gap pyrazoline scaffold: The critical role of a para-nitro substituent. Multidisciplinary Surgical Research Annals, 2025, 3(3), 461-503.

[21] Abbas MA, Mahar J, Rasool MS, Khan MJ, Khan MZ. The dual therapeutic promise of quinoa: Exploring antidiabetic and antioxidant effects through experimental and computational models. Multidisciplinary Surgical Research Annals, 2025, 3(3), 504-544.

[22] Abbas MA, Mahar J, Khan MJ. Rasool MS, Khan MZ. *In silico* investigation of 3, 6-diphenyl-[1,2,4] triazolo [3,4-B][1,3,4] thiadiazole derivatives as egfr modulators for lung cancer treatment.The Cancer Research Review, 2025, 4(2), 243-308. DOI: 10.5281/zenodo.17044904

[23] Abbas MA. Advanced synthesis and multifunctional characterization of neodymium-doped $Ba_2NiCoFe_{28-x}O_{46}$ X-type hexagonal ferrites: A comprehensive study of structural, Morphological, and electromagnetic properties. Scholars Academic Journal of Biosciences, 2025, 8, 1213-1227. DOI: 10.36347/sajb.2025.v13i08.014

[24] Huang H, He Y, Li X, Li M, Zeng C, Dong F, et al. Bi_2O_2 (OH)(NO_3) as a desirable $[Bi_2O_2]^{2+}$ layered photocatalyst: Strong intrinsic polarity, rational band structure and {001} active facets co-beneficial for robust photooxidation capability. Journal of Materials Chemistry A, 2015, 3(48), 24547-24556. DOI: 10.1039/C5TA07655B

[25] Iqbal MT, Saeeda S, Zahra T, Umar Z, Khan WZ, Adnan M, et al. Next-generation materials discovery using DFT: Functional innovation. Scholars Journal of Engineering and Technology, 2025, 7, 454-486. DOI: 10.36347/sjet.2025.v13i07.003

[26] Ahmed A, Fatima A, Shakya S, Rahman QI, AhmadM, Javed S, et al. Crystal structure, topology, DFT and Hirshfeld surface analysis of a novel charge transfer complex (L3) of anthraquinone and 4–{[(anthracen–9–yl) meth–yl] amino}–benzoic acid (L2) exhibiting photocatalytic properties: An experimental and theoretical approach. Molecules, 2022, 27(5), 1724. DOI: 10.3390/molecules27051724

[27] Li K, He Y, Chen P, Wang H, Sheng J, Cui W, et al. Theoretical design and experimental investigation on highly selective Pd particles decorated C_3N_4 for safe photocatalytic NO purification. Journal of Hazardous Materials, 2020, 392, 122357. DOI: 10.1016/j.jhazmat.2020.122357

[28] Oliveira MC, Fonseca VS, Neto NFA, Ribeiro RAP, Longo E, De Lazaro SR ,et al. Connecting theory with experiment to understand the photocatalytic activity of CuO–ZnO heterostructure. Ceramics International, 2020, 46(7), 9446-9454. DOI: 10.1016/j.ceramint.2019.12.205

[29] Li X, Maffettone PM, Che Y, Liu T, Chen L, Cooper AI. Combining machine learning and high-throughput experimentation to discover photocatalytically active organic molecules. Chemical Science, 2021, 12(32), 10742-10754. DOI: 10.1039/D1SC02150H

[30] Mai H, Le TC, Chen D, Winkler DA, Caruso RA. Machine learning for electrocatalyst and photocatalyst design and discovery. Chemical Reviews, 2022, 122(16), 13478-13515. DOI :10.1021/acs.chemrev.2c00061

[31] Hussain S, Rehman JU. First-principles calculations to investigate structural, electronics, mechanical, and optical properties of KGaO3 cubic perovskite for photocatalytic water-splitting application. Optik, 2023, 291, 171326. DOI: 10.1016/j.ijleo.2023.171326

[32] Ni Q, Ke X, Qian W, Yan Z, Luan J, Liu W. Insight into tetracycline photocatalytic degradation mechanism in a wide pH range on BiOI/BiOBr: Coupling DFT/QSAR simulations with experiments. Applied Catalysis B: Environmental, 2024, 340, 123226. DOI: 10.1016/j.apcatb.2023.123226

[33] Duan X, Huang Y, Shen C, Jones P, Deng X. Study on the sterilization performance of photocatalysts used in indoor air purification. Indoor Air, 2025, 2025(1), 1071778. DOI: 10.1155/ina/1071778

[34] Xia Y, Yang H, Ho W, Zhu B, Yu J. Promoting the photocatalytic NO oxidation activity of hierarchical porous g–C_3N_4 by introduction of nitrogen vacancies and charge channels. Applied Catalysis B: Environment and Energy, 2024, 344, 123604. DOI: 10.1016/j.apcatb.2023.123604

[35] Pingak RK, Conquest OJ, Stampfl C. A DFT investigation of photocatalytic water splitting properties of the InS/GaTe heterostructure: Direct Z-scheme vs. traditional type-II. Journal of Materials Chemistry A, 2025, 13(44), 38350-38368. DOI: 10.1039/D5TA04464B

[36] Zhang X, Chen A, Chen L, Zhou Z. 2D materials bridging experiments and computations for electro/photocatalysis. Advanced Energy Materials, 2022, 12(4), 2003841. DOI: 10.1002/aenm.202003841

[37] Alharshan GA, Aboraia AM, Uosif MAM, Sharaf IM, Shaaban ER, Saad M, et al. Optical band gap tuning, DFT understandings, and photocatalysis performance of ZnO nanoparticle-doped Fe compounds. Materials, 2023, 16(7), 2676. DOI: 10.3390/ma16072676

[38] Liu H, Pan L, Nie J, Mei H, Zhu G, Jin Z, et al. $Bi_{12}TiO_{20}$–TiO_2 S-scheme heterojunction for improved photocatalytic NO removal: Experimental and DFT insights. Separation and Purification Technology, 2023, 314, 123575. DOI: 10.1016/j.seppur.2023.123575

[39] Bisht A, Kamboj N, Kamboj V, Bisht A. A review on the role of emerging anthropogenic activities in environmental degradation and emphasis on their mitigation. Archives of Agriculture and Environmental Science, 2020, 5(3), 419-425. DOI: 10.26832/24566632.2020.0503025

[40] Thawarkar S, Rondiya SR, Dzade NY, Khupse N, Jadkar S. Experimental and theoretical investigation of the structural and opto-electronic properties of Fe-doped lead-free $Cs_2AgBiCl_6$ double perovskite. Chemistry-A European Journal, 2021, 27(26), 7408-7417. DOI: 10.1002/chem.202004902

Table S1. DFT-optimized bond lengths and bond angles of MO and Ag–Co_3O_4@MO.

MO	Bond length	MO	Bond angles	Ag–Co_3O_4@MO	Bond length	Ag–Co_3O_4@MO	Bond angles
S17Na1	2.753	C14S17Na1	125.174	C6C5	1.424	C7C6C5	120.824
C14S17	1.83	O18S17Na1	52.239	C7C6	1.377	C8C7C6	120.884
O18S17	1.643	O20S17Na1	51.886	C8C7	1.408	C22C5C6	117.455
O20S17	1.642	C13C14S17	119.425	C22C5	1.428	C21C22C5	121.332
C13C14	1.385	C15C14C13	122.579	C21C22	1.378	N9C8C7	115.177
C15C14	1.388	C12C13C14	118.483	N9C8	1.394	N10N9C8	120.02
C12C13	1.391	C11C12C13	120.348	N10N9	1.304	C11N10N9	105.99
C11C12	1.403	C16C15C14	118.812	C11N10	1.452	C12C11N10	118.086
C16C15	1.388	N10C11C12	115.758	C12C11	1.408	C16C11C12	120.911
N10C11	1.426	N9N10C11	113.601	C16C11	1.399	C13C12C11	118.858
N9N10	1.299	C8N9N10	114.973	C13C12	1.395	C15C16C11	118.412
C8N9	1.406	C7C8N9	116.78	C15C16	1.398	C14C15C16	118.521
C7C8	1.404	C21C8C7	118.141	C14C15	1.389	S17C14C13	114.803
C21C8	1.407	C6C7C8	121.462	S17C14	1.847	O18S17C14	96.988
C6C7	1.383	C5C6C7	120.852	O18S17	1.683	O20S17O18	103.465
C5C6	1.42	C22C21C8	121.096	O20S17	1.627	Na1O20S17	93.818
C22C21	1.379	N3C5C6	121.465	Na1O20	2.279	N3C5C6	121.355
N3C5	1.375	H29C6C5	120.036	N3C5	1.368	O19S17C14	111.683
H29C6	1.08	H30C7C6	120.761	O19S17	1.581	H29C6C5	120.146
H30C7	1.083	H31C12C11	117.976	H29C6	1.08	H30C7C6	121.733
H31C12	1.082	H32C13C12	122.668	H30C7	1.088	H31C12C11	120.465
H32C13	1.082	H33C15C14	118.797	H31C12	1.083	H33C15C14	119.347
H33C15	1.083	H34C16C11	118.103	H33C15	1.085	H34C16C11	119.878
H34C16	1.081	H35C21C8	117.799	H34C16	1.083	H36C22C5	119.683
H35C21	1.082	H36C22C5	119.75	H36C22	1.08	O39Na1O18	97.637
H36C22	1.081	O19S17Na1	127.921	O39Na1	2.133	H32C13C12	121.161
O19S17	1.585	C2N3C5	120.399	H32C13	1.085	H35C21C8	118.805
C2N3	1.472	C4N3C2	119.383	H35C21	1.082	C2N3C5	120.55
C4N3	1.471	H23C2N3	108.665	C2N3	1.474	C4N3C2	119.163
H23C2	1.091	H24C2N3	111.448	C4N3	1.475	Co37O39Na1	130.446
H24C2	1.098	H25C2N3	111.452	Co37O39	1.595	O38Co37O39	142.388
H25C2	1.098	H26C4N3	108.722	O38Co37	1.558	Ag40Co37O38	87.219
H26C4	1.091	H27C4N3	111.395	Ag40Co37	2.499	H23C2N3	108.617
H27C4	1.098	H28C4N3	111.408	H23C2	1.09	H24C2N3	111.313
H28C4	1.098			H24C2	1.097	H25C2N3	111.273
				H25C2	1.097	H26C4N3	108.664
				H26C4	1.09	H27C4N3	111.117
				H27C4	1.097	H28C4N3	111.316
				H28C4	1.097		

Table S2. DFT-derived FMO energies and global reactivity descriptors of MO and Ag–Co_3O_4@MO.

Parameter	MO	Ag–Co_3O_4@MO	Unit
HOMO (EH)	−5.24	−5.80	eV
LUMO (EL)	−2.02	−2.69	eV
Energy Gap ($\Delta E_{(gap)}$)	3.22	3.11	eV
Ionization Potential (IP)	5.24	5.80	eV
Electron Affinity (EA)	2.02	2.69	eV
Electronegativity (χ)	3.63	4.25	eV
Chemical Potential (μ)	−3.63	−4.25	eV
Hardness (η)	1.61	1.56	eV
Softness (S)	0.31	0.32	eV^{-1}
Electrophilicity (ω)	4.09	5.78	eV